

Scalable High-Performance Nanolaminated SERS Substrates Based on Multistack Vertically Oriented Plasmonic Nanogaps

Junyeob Song, Wonil Nam, and Wei Zhou*

Metallic nanogap structures can support gap surface plasmon modes and strongly concentrate optical fields to enable surface-enhanced Raman spectroscopy (SERS) for label-free biochemical analysis down to single molecule level. However, current scalable SERS substrates based on horizontally oriented plasmonic nanogaps still face challenges for accurate sub-10 nm control of in-plane nanostructures. Here, we report a new type of scalable high-performance SERS substrate based on multistack vertically oriented nanogap hotspots in metal–insulator–metal nanolaminated plasmonic crystals. In contrast to horizontally oriented nanogaps, vertically oriented plasmonic nanogaps can be controlled at subnanometer resolution in the multilayered thin-film deposition process. After a partial etching of dielectric layers, embedded nanogap hotspots in nanolaminated SERS substrates can be exposed to further increase SERS enhancement factors (EFs) by over one order of magnitude from $\approx 1 \times 10^7$ to $\approx 1.6 \times 10^8$. Moreover, oxygen plasma can be used to regenerate clean nanogap hotspots for repeated SERS measurements with maintained high SERS EFs ($> 1 \times 10^8$). Therefore, this work presents a novel out-of-plane plasmonic engineering approach to design and manufacture scalable high-performance reusable SERS substrates for various biochemical analysis applications that prefer high spatial-temporal resolution and good hotspot uniformity.

Since its discovery in the 1970s,^[1] surface-enhanced Raman spectroscopy (SERS) has emerged as a promising label-free analytical technique to provide chemical fingerprint information for applications ranging from molecular detection and profiling, to cellular identification and classification, and to food and environmental monitoring.^[2] By surface plasmon enhancement of both excitation and inelastic scattering processes of analyte molecules in hotspots, nanoplasmonic SERS substrates can achieve the molecule ensemble average SERS enhancement factors (EFs) above 10^7 , sufficient for single molecule detection.^[3,4] Compared to uncoupled plasmonic nanostructures, strongly coupled plasmonic nanostructures with nanoscale separations

can support gap plasmon modes with much tighter optical field confinement in nanogaps,^[5] and thus can produce much higher SERS EFs theoretically up to 10^{10} .^[6] Experiments have demonstrated that plasmonic nanogaps based on metal nanoparticle aggregations possess single molecule SERS detection capabilities.^[7] However, the hotspots in bottom-up assembled nanoparticle aggregations show a random and uncontrollable distribution because of the extremely sensitive dependence of gap plasmon resonances on nanogap dimensions. Calculations have illustrated that SERS enhancement factors for coupled metal nanostructures can change by five orders of magnitude with a nanogap variation less than 10 nm.^[8]

Toward controlled engineering of plasmonic nanogap hotspots, significant efforts have been made to create high-performance uniform SERS substrates using scalable nanofabrication strategies. Based on the orientation of plasmonic nanogaps, SERS substrates can be further classified into two types: 1) horizontally oriented nanogap structures where the dominant electric field is parallel to the substrate surface and 2) vertically oriented nanogap structures where the dominant electric field is perpendicular to the substrate surface. Since it is more straightforward to create horizontally oriented plasmonic nanogaps by modifying lithography defined in-plane nanopatterns, most top-down fabricated SERS substrates exploit horizontally oriented nanogap hotspots typically with SERS EFs on the order of 10^6 – 10^7 .^[9–13] However, for sub-10 nm control of horizontally oriented plasmonic nanogaps, most of these works require the use of nonstandard fabrication techniques to go beyond the nanolithography resolution limit, such as microcapillary forces driven nanogap generation by self-coalescence of nanopillar arrays,^[9] ion-milling or adhesive-stripping assisted exposure of atomic layer deposition defined nanogaps,^[10] self-aligned generation of nanogaps by off-angle shadow deposition through nanomasks,^[11] and thermal annealing-assisted nanogap generation by forming metal nanoislands between nanopillar arrays.^[12] Therefore, despite significant improvement, current scalable SERS substrates by engineering horizontally oriented plasmonic nanogaps still face challenges in relatively high fabrication costs and limited spectral

J. Song, W. I. Nam, Prof. W. Zhou
Department of Electrical and Computer Engineering
Virginia Tech
Blacksburg, VA 24060, USA
E-mail: wzh@vt.edu

 The ORCID identification number(s) for the author(s) of this article can be found under <https://doi.org/10.1002/admt.201800689>.

DOI: 10.1002/admt.201800689

controllability of gap plasmon modes for SERS operation in the near-infrared (NIR) biological window. On the other hand, although many studies have demonstrated the good SERS performance of vertically oriented plasmonic nanogaps in bottom-up assembled nanoparticle-nanogap-mirror structures,^[14] little progress has been made in high-throughput fabrication of uniform SERS substrates by engineering vertically oriented plasmonic nanogaps.

In this work, we report a new type of scalable high-performance SERS substrates based on multistack vertically oriented nanogap hotspots in nanolaminated plasmonic crystals, which can be manufactured in a high-throughput top-down approach, can have a uniform distribution of hotspots with SERS EFs on the order of 10^8 , and can be reused simply after a short oxygen plasma cleaning process. As illustrated in **Figure 1A**, a single unit cell of the nanolaminated plasmonic crystals can contain multiple vertically stacked metal-insulator-metal (MIM) nanocavities supporting gap plasmons with highly concentrated optical fields and by partial etching of insulator layers of MIM nanocavities, the embedded vertically oriented plasmonic nanogap hotspots can be exposed for high-performance SERS detection of analyte molecules in the environment. Compared to conventional SERS substrates based on horizontally oriented plasmonic nanogaps, our novel nanolaminated SERS

substrates based on multistack vertically oriented nanogap hotspots provide some unique opportunities.^[15,16] First, it is much easier to achieve accurate nanoscale geometric control of vertically oriented plasmonic nanogaps in terms of film thicknesses than to define horizontally oriented nanogap geometries by lithography-based processes. Second, by adjusting film thicknesses of MIM building blocks in the vertical stack, we can easily tune the resonant response of nanolaminated SERS substrates to operate under NIR laser excitation for applications requiring low autofluorescence, reduced cellular phototoxicity, and deep light penetration in biological tissues. Finally, by relaxing the degree of freedom in multiple out-of-plane geometric parameters, MIM nanolaminated plasmonic nanostructures can be engineered to have multiresonant optical properties for wavelength-multiplexed operations,^[15] which will allow for combining SERS with other optical sensing or actuation modalities under different excitation wavelengths in a spatiotemporally correlated manner.

Figure 1B illustrates the top-down fabrication process to create scalable nanolaminated SERS substrates. Briefly, we first used a nanostructured polydimethylsiloxane (PDMS) stamp to replicate polymer nanopillar arrays on polyester (PET) films with a UV curable polyurethane (PU) polymer resist. Next, we deposited alternating layers of Au and SiO_2 films to create

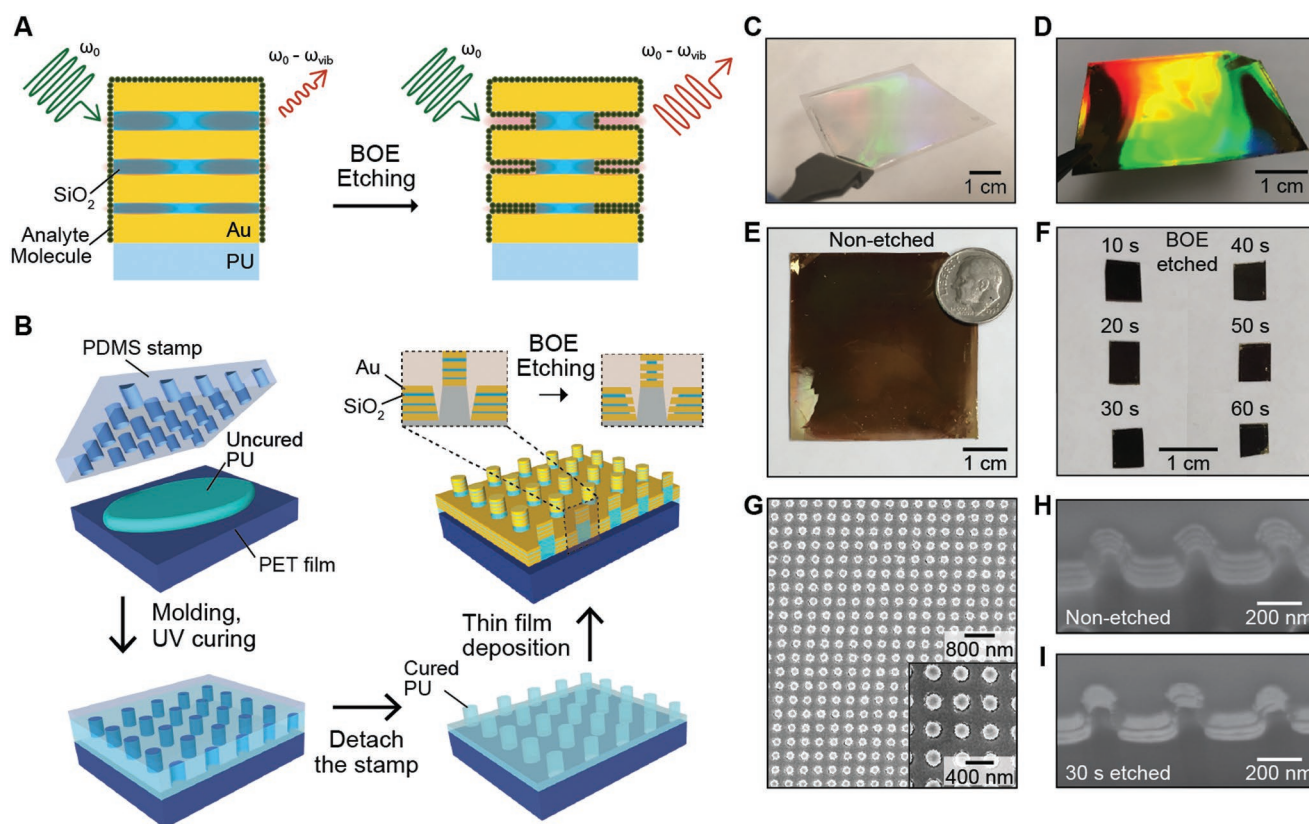


Figure 1. Scalable high-performance nanolaminated SERS substrates. A) Schematic illustration of increased Raman signal intensity ($\omega_0 - \omega_{\text{vib}}$) of analyte molecules on the surface of the nanolaminated plasmonic crystals after exposing multistack vertically oriented plasmonic nanogap hotspots by BOE etching of the insulator layers. B) Schematic representation for fabricating nanolaminated SERS substrates with three insulator layers. C, D) Tilted-view optical images of substrate C) before and D) after the MIM deposition process. E) Top-view optical image of the nanolaminated SERS substrate. F) Optical image of nanolaminated SERS substrate samples with different BOE etching times. G) Top-view SEM image of a nonetched nanolaminated SERS substrate. H, I) Cross-sectional view SEM images of nanolaminated SERS substrates with H) 0 s (nonetched) and I) 30 s BOE etching.

multilayered MIM nanostructures with multistack vertically oriented plasmonic nanogaps on individual nanopillars by electron-beam deposition. Finally, we used a wet chemical etching process to expose embedded nanogap hotspots with buffered oxide etchant 10:1 (BOE) for improving the SERS performance. Figure 1C,D shows the optical images of samples before and after the deposition of alternating MIM films on nanopillar arrays on the flexible PET substrate. We can observe strong light diffraction patterns from both samples over large areas, indicating a uniform distribution of periodic nanostructures on the substrates. The dark appearance of the fabricated SERS substrate from the top-view optical image (Figure 1E) reflects a broadband absorption in visible frequencies. Figure 1F shows a similar dark appearance between six SERS substrate samples under different etching times from 10 to 60 s, indicating a good structural stability of vertically stacked MIM nanocavities in the BOE etching process. Figure 1G,H shows top-view and cross-sectional scanning electron microscopy (SEM) images of nanolaminated SERS substrates without BOE etching. According to the design of composite MIM nanoantennas in our previous work,^[16] we deposited four Au layers with the same thickness of 30 nm and three SiO₂ layers with different thicknesses of 6, 8, and 12 nm from bottom to top. The inversely tapered shape of multilayered MIM nanostructures on nanopillars is attributed to the shadowing effect from the line-of-sight electron-beam deposition process. After 30 s BOE etching (Figure 1I), the multilayered nanostructures on nanopillars show an increased side-wall surface roughness and a reduced total height due to the partial removal of SiO₂ layers in the nanogaps.

To study the effect of BOE etching on the optical properties of nanolaminated plasmonic crystals, we measured normal-incidence reflectance spectra of samples under different etching times (Figure 2A). Before being etched, the nanolaminated plasmonic crystals exhibit rich multiresonant optical properties featured by multiple reflection dips due to the absorption of different plasmon modes at 630, 690, 770, 810, 990, and 1400 nm,

while the absorption feature below 530 nm is associated with interband electronic transitions in Au. After being etched at 30 and 60 s, the reflectance spectra of samples changed accordingly due to the changes of local dielectric configurations and geometries of multistacked nanogaps in nanolaminated plasmonic crystals (also shown in their cross-sectional SEM images, Figure 2A). In particular, with the etching time increased from 0 to 30 and to 60 s, the resonant dip initially at 1400 nm blueshifted to 1130 and to 1015 nm with a reduced amplitude and the resonant dip initially at 990 nm blueshifted and merged with the other resonance at 850 nm.

For a better understanding of observed resonant features and their dependence on the etching process, we used 3D finite-difference time-domain (FDTD) method to calculate far-field and near-field optical properties of nanolaminated plasmonic crystals with different volume etching ratios of dielectric layers in the nanogaps. In good agreement with the measurements, the FDTD calculated reflectance spectrum of the nonetched sample exhibits plasmonic resonant dips at 615, 675, 750, 860, 995, and 1400 nm. From calculated near-field profiles, these modes show intense optical fields in dielectric nanogaps between metal layers as well as in the vicinity of periodic plasmonic nanohole arrays (Figure S1, Supporting Information), which is a result of optical hybridization between localized gap plasmon modes in MIM nanostructures and delocalized surface plasmon polariton Bloch-modes in periodic plasmonic structures. To numerically model the etching effect on their optical properties, we performed FDTD calculations of nanolaminated plasmonic crystals with increased volume ratio of air ($n = 1$) in nanogap layers from 0%, to 15%, and to 30%. As shown in Figure 2B, with increasing etching ratios, the reflection dip initially at 1400 nm (nonetched) blueshifts to 1350 nm (15% etched) and to 1320 nm (30% etched), and the dip initially at 860 nm (non-etched) blueshifts to 810 nm (15% etched) and to 780 nm (30% etched). Despite the qualitative agreement in the blueshifting trend of gap plasmons by reducing the effective/average

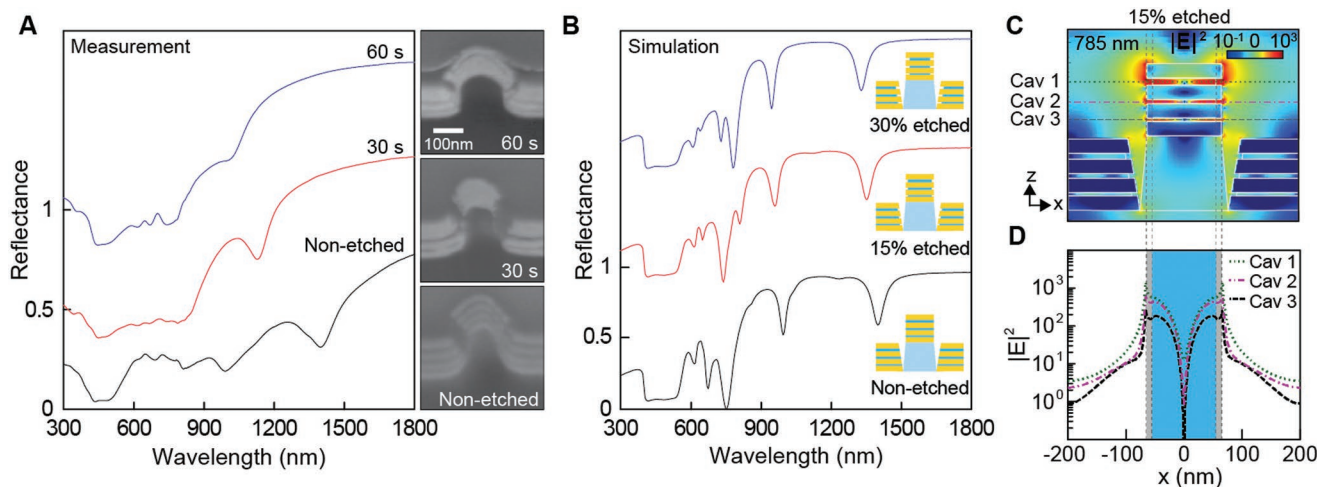


Figure 2. Optical properties of nanolaminated plasmonic crystals. A) Measured reflectance spectra and corresponding SEM cross-sectional images of nanolaminated plasmonic crystals with different BOE etching times of 0 (nonetched), 30, and 60 s. B) FDTD-calculated reflectance spectra of nanolaminated plasmonic crystals with different etching volumes of insulator layers (nonetched, 15% etched, and 30% etched). The inset cartoons illustrate their corresponding unit cell geometries. C) The FDTD-calculated x - z distribution map (785 nm) of $|E|^2$ for the nanolaminated plasmonic crystal with 15% etching volumes of insulator layers. D) The FDTD-calculated $|E|^2$ as a function of x for the three MIM plasmonic nanogap cavities in the vertical stack.

refractive index in the nanogaps, the calculations show much smaller changes of mode wavelengths and reflectance dip amplitudes compared to the measurements. This discrepancy is mainly because the model in FDTD calculations cannot capture the additional geometric deformation of partially etched MIM nanostructures driven by the nanocapillary force during etching, rinsing, and drying processes.

To estimate the local field concentration in multistacked nanogaps of nanolaminated plasmonic crystals for SERS applications under 785 nm NIR laser excitation, we calculated the distribution map of electric field intensity $|E|^2$ at 785 nm for the sample with a 15% etching ratio (Figure 2C). In Figure 2D, we depict $|E|^2$ at different locations along x axis across the middle line of nanogaps for three MIM nanocavities in the vertical stack. As $|x|$ increases from 0 to 200 nm, $|E|^2$ first increases gradually in the embedded nanogap regions (blue) and reaches the maximum in the exposed nanogap regions (gray), and then drops quickly outside nanogaps (white). The peak values of $|E|^2$ in exposed nanogaps from top to bottom are 1.4×10^3 , 6.8×10^2 , and 2.0×10^2 , respectively, and their SERS EFs can be estimated as 2.0×10^6 , 4.6×10^5 , and 4.1×10^4 according to the $|E|^4$ approximation.^[17] Therefore, our numerical calculations predict it is possible to transform the embedded “passive” hotspots into exposed “active” hotspots by partial etching of dielectric layers in MIM plasmonic nanocavities.

By measuring Raman spectra of benzenethiol (BZT) molecules assembled on nanolaminated plasmonic crystals with different etching times, we have demonstrated a significant improvement of their SERS performance by physically exposing embedded nanogap hotspots. Figure 3A shows that

BZT SERS signals first quickly rise and reach a maximum with BOE etching time increased from 0 to 30 s and then gradually fall with the etching time increased from 30 to 60 s. In Figure 3A, each Raman spectrum was acquired by averaging Raman signals from 400 pixels over a $5 \mu\text{m} \times 5 \mu\text{m}$ area under 785 nm laser excitation using a confocal Raman spectromicroscopy system. The five major peaks at 422, 1001, 1026, 1077, and 1576 cm^{-1} correspond to the carbon-sulfur (C-S) stretching and carbon-carbon-carbon (C-C-C) ring in-plane deformation vibration, the C-C-C ring in-plane bending mode, the carbon-hydrogen (C-H) in-plane bending mode, the C-C-C ring in-plane breathing mode with C-S stretching mode, and the C-S stretching mode for BZT molecules.^[18] The sample with 30 s BOE etching shows an optimized SERS performance with 17 times higher Raman signal intensity (1077 cm^{-1}) than the nonetched one. With the etching time increased from 30 to 60 s, the SERS performance gradually decreased, which however, is still five times better than the nonetched one. Our corroborated observations from SEM, reflectance, and SERS measurements suggest that the geometric deformation of nanolaminated plasmonic nanostructures due to the BOE etching process is likely self-limited and can still result in a better SERS performance than nonetched samples by increasing the nanoscale sidewall roughness.

Figure 3B shows the 2D confocal Raman images (at 1077 cm^{-1}) over a $5 \mu\text{m} \times 5 \mu\text{m}$ area for samples with etching times of 0, 30, and 60 s. We collected the Raman signals using a $100\times$ objective lens with a numerical aperture (NA) of 0.9. To study the uniformity of SERS hotspots on nanolaminated plasmonic crystals under different etching conditions, we

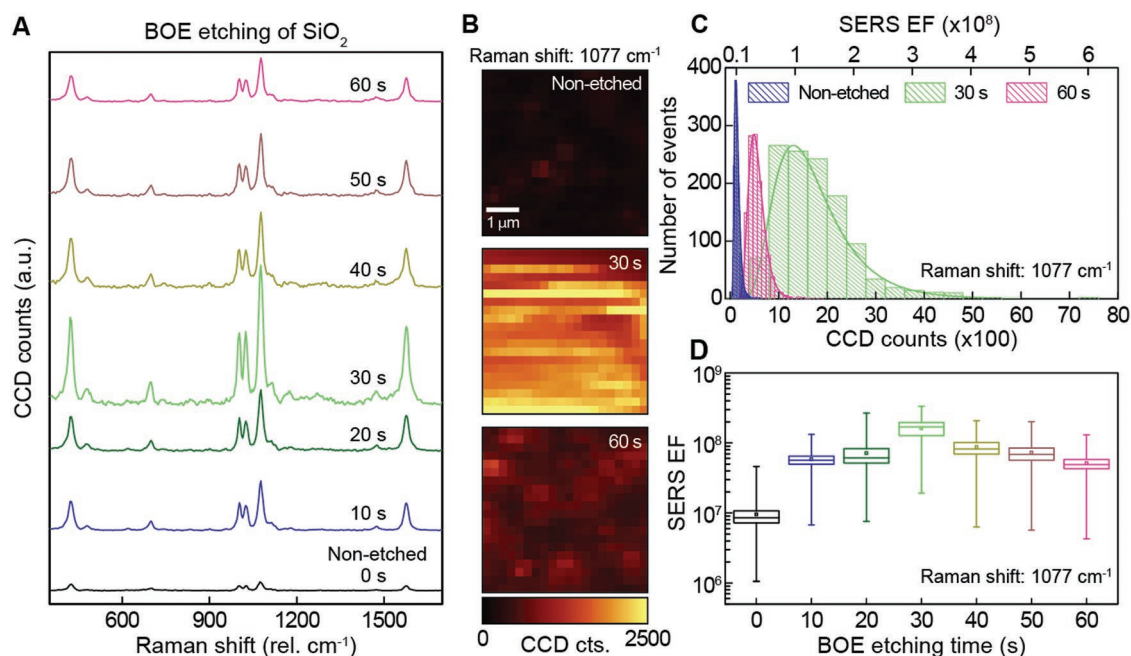


Figure 3. SERS performance of nanolaminated plasmonic crystals. A) The measured Raman spectra of BZT molecules assembled on the surface of nanolaminated plasmonic crystals with different BOE etching times under 785 nm laser excitation. B) Scanning confocal Raman images (1077 cm^{-1}) of nanolaminated plasmonic crystals with 0, 30, and 60 s BOE etching. C) Histograms of Raman signal intensities and corresponding SERS EFs (1077 cm^{-1}) for nanolaminated plasmonic crystals with 0, 30, and 60 s BOE etching. D) The SERS EFs (1077 cm^{-1}) of nanolaminated plasmonic crystals with different etching times. The five different bars from top to bottom represent the max, 75%, median, 25%, and min values of SERS EFs respectively; and the square box represents the mean value.

plotted the histograms of 1077 cm^{-1} Raman signal intensities and corresponding SERS EFs from 1200 pixels sampled in three different areas (Figure 3C). The SERS EFs were calculated by the formula: $EF = (I_{\text{SERS}}/I_{\text{Raman}}) \times (N_{\text{Raman}}/N_{\text{SERS}})$ (see details in the Experimental Section).^[4] Samples for three different etching times all show a log-normal distribution of SERS EFs with a peak position adjacent to the mean value, which indicates a uniform distribution of hotspots on the SERS substrates.^[19] Relative standard deviation (RSD) values of SERS EFs for samples with etching times at 0 (nonetched), 30, and 60 s are 28.8%, 28.12%, and 37.33%, respectively. The slight $\approx 10\%$ increase of RSD for the sample with a 60 s etching time also reflects the random but self-limited nature

of the etching-induced geometric deformation process for multilayered MIM nanostructures. It should be noted that the RSD values of SERS EFs also depend on the NA of the objective lens used in the Raman measurement, and a less focused beam due to a smaller NA can include more hotspots for spatial averaging in each pixel and thus reduce RSD values for the same sample.^[20] Figure 3D shows the plots of measured SERS EFs for the samples with different etching times. With increased etching times, the average SERS EFs of samples rapidly increase from 9.7×10^6 (0 s, nonetched) to the maximum value 1.6×10^8 (30 s, etched), and then gradually decrease to 5.2×10^7 (60 s, etched). To the best of our knowledge, the measured SERS EFs of $\approx 1.6 \times 10^8$ from our nanolaminated

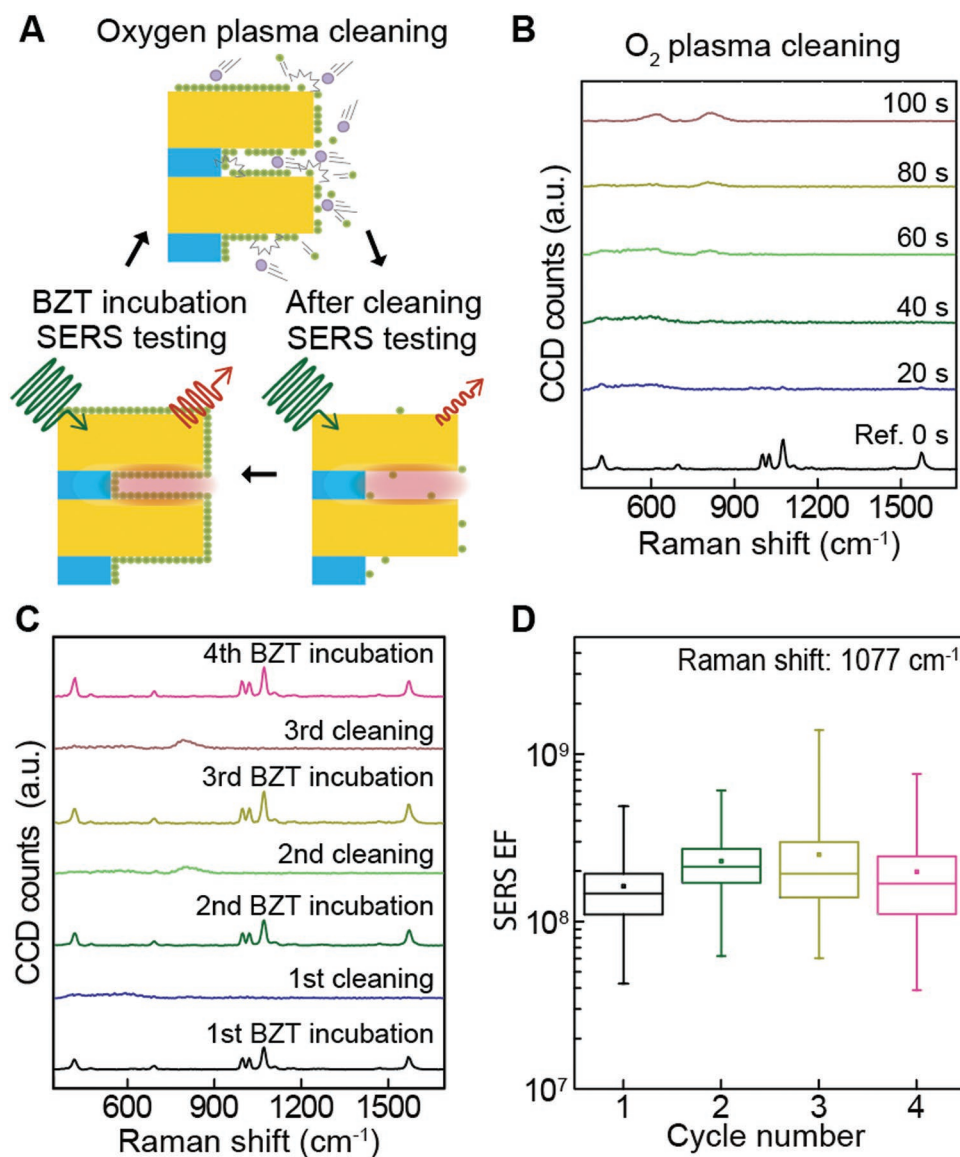


Figure 4. Reusability of nanolaminated SERS substrates. A) Schematic illustration of the oxygen plasma cleaning of BZT molecules in nanogap hotspots for repeated SERS measurements. B) Evolution of Raman spectra from the same BZT assembled SERS substrate at different oxygen plasma cleaning times. C) Measured Raman spectra from the same SERS substrate after different cycles of BZT incubating and oxygen plasma cleaning. D) The SERS EFs of the same nanolaminated SERS substrate (1077 cm^{-1}) in four cycles of BZT SERS measurements after oxygen plasma regeneration. The five different bars from top to bottom represent the max, 75%, median, 25%, and min values of SERS EFs respectively; and the square box represents the mean value.

plasmonic crystals are among the highest reported in literature for scalable uniform SERS substrates made of biocompatible Au under the NIR laser excitation.

Last, we have explored the reusability of nanolaminated plasmonic crystals for repeated SERS measurements by regenerating fresh hotspots using the oxygen plasma cleaning process. **Figure 4A** shows the schematic illustration of one cycle in repeated SERS measurements, in which accelerated radicals in the oxygen plasma can remove BZT molecule layers from the surface of plasmonic nanostructures via chemical reaction and physical bombardment processes. **Figure 4B** shows the evolution of Raman spectra from BZT assembled SERS substrates (with 30 s BOE etching) after being treated in the oxygen plasma (RF power: 50 W, O₂ gas flow: 50 sccm) with different cleaning times, ranging from 0 s (reference) to 100 s. We find that BZT SERS signals can be reduced by two orders of magnitude after 20 s oxygen plasma cleaning and can be totally eliminated after 40 s oxygen plasma cleaning. Interestingly, as the oxygen plasma cleaning time was further increased from 40 to 100 s, two very broad Raman peaks at 620 and at 814 cm⁻¹ emerged and kept increasing in amplitude. We suspect that these broad Raman features are likely from amorphous-like byproduct materials generated and deposited in plasmonic nanogap hotspots during physical and chemical interactions between oxygen plasma and PU polymer nanopillars under multilayered plasmonic nanostructures. **Figure 4C** shows that nanolaminated plasmonic crystals can be used for repeated BZT SERS measurements by a 40 s oxygen plasma cleaning in four experimental cycles. Moreover, we find that the broad Raman peak at 814 cm⁻¹ emerging after the second and third rounds of oxygen plasma cleaning disappears in the SERS measurements after the third and fourth rounds of BZT incubation and ethanol rinsing process, indicating that the byproduct materials deposited in nanogap hotspots during oxygen plasma cleaning process are weakly physisorbed and thus can be simply washed away in the liquid environments. To have a quantitative assessment of the change of SERS performance for nanolaminated plasmonic crystals after multiple cycles of reusability testing experiments, we plotted the dependence of SERS EF distributions measured from 400 pixels on the cycle number (**Figure 4D**). We find that the same sample after multiple cycles of usage can maintain very high SERS EFs (2.3×10^8 , 2.5×10^8 , and 2.0×10^8) even slightly higher than its first usage (1.8×10^8), while its RSD (38%, 69%, and 62%) increases slightly due to accumulated mechanical perturbations to the nanogap hotspots in the plasma cleaning, liquid rinsing, and air drying processes.

In summary, we have demonstrated a new type of scalable high-performance SERS substrates based on multistack vertically oriented plasmonic nanogap hotspots in nanolaminated plasmonic crystals, which can be manufactured in a high-throughput top-down fabrication process for mass production. By partial wet etching of dielectric nanogap layers, we can expose embedded nanogap hotspots to further increase SERS EFs by over one order of magnitude from $\approx 9.6 \times 10^6$ to $\approx 1.6 \times 10^8$. Moreover, due to their chemical and mechanical stability, nanolaminated plasmonic crystals show an excellent reusability for repeated SERS measurements simply by oxygen plasma cleaning. Compared to most SERS substrates by horizontally oriented nanogap engineering, nanolaminated SERS

substrates based on multistack vertically oriented plasmonic nanogaps have several advantages: 1) accurate nanoscale control of vertically oriented plasmonic nanogap geometries based on film thicknesses, 2) compatible with scalable high-throughput fabrication process, 3) good spectral tunability of out-of-plane nanogap plasmons for biological SERS applications requiring the NIR laser excitation, and 4) capable for wavelength-multiplexed multimodal operation by out-of-plane engineering of individual MIM nanocavities in the vertical stack. Therefore, scalable high-performance nanolaminated SERS substrates are very promising for real-time label-free biochemical monitoring of dynamic and complex bio/chemical systems with high spatial-temporal resolution and good sensitivity.

Experimental Section

Fabrication of Nanolaminated Plasmonic Crystals: A composite PDMS mold was fabricated from a silicon master consisting of a 2D square periodic array of nanopillars (periodicity: 400 nm, diameter: 100 nm, and height: 400 nm).^[21] Polymer nanopillar arrays were replicated from the PDMS mold on a PET film using PU UV-curable polymer (NOA 83H, Norland Product Inc., USA). PU was squeezed between the mold and PET film, and cured by UV for 10 min followed by postannealing process (overnight at 80 °C). Alternating layers of Au layers (30 nm) and SiO₂ layers (6, 8, and 12 nm from bottom) were deposited on the PU pillar arrays using e-beam evaporation (PVD250, Kurt J. Lesker, USA). In addition, 1 nm of chromium on nanopillar arrays and 0.7 nm of titanium between Au and SiO₂ layers were deposited as adhesion layers. To open the dielectric nanogaps, BOE 10:1 was used (Transene Inc., USA). The reflectance spectra were measured by a UV–vis–NIR spectrophotometer (Cary 5000, Agilent, USA).

Finite-Difference Time-Domain Simulation: 3D FDTD simulations were performed by a commercial software (FDTD solution, Lumerical Inc., Canada). A uniform 2 nm mesh was used to x-, y-, and z-directions. The optical constants of Au were taken from Johnson and Christy.^[22] The Bloch boundary condition was used in x- and y-directions with a periodicity of 400 nm and the perfectly matched layer boundary condition was used in the z-direction. The refractive indices of SiO₂ and PU were set as 1.5 and 1.56, respectively.

Raman Measurement: To evaluate the SERS performance of samples, BZT (Sigma-Aldrich, USA) was used as the probe molecules. To form a self-assembled monolayer, samples were incubated in 1×10^{-3} M of BZT ethanolic solution for 24 h followed by ethanol rinsing. For Raman measurement, a confocal Raman microscope (alpha 300 RSA+, WITec, Germany) equipped with a 785 nm diode laser (Xtra II, Toptica, Germany) was used. Signals were collected via 100× objective lens with 0.7 mW and 1 s integration time. The backscattered photons were detected by a spectrometer (UHTS300, WITec, Germany) equipped with a CCD camera (DU401A, Oxford instruments, UK). After signal acquisition, cosmic rays removal and baseline correction were performed by a software (Project v4.1, WITec, Germany).

EF Calculation: The SERS EFs were calculated by, $EF = (I_{SERS}/I_{Raman}) \times (N_{Raman}/N_{SERS})$. I_{SERS} , I_{Raman} , N_{SERS} , and N_{Raman} are the SERS BZT intensity, neat BZT Raman intensity, and the number of BZT molecules contributing to SERS and neat Raman intensities, respectively.^[3] I_{SERS} (1077 cm⁻¹) and I_{Raman} (1094 cm⁻¹) were measured, which are C-C-C ring in-plane breathing mode with C-S stretching mode (**Figure S2**, Supporting Information).^[18,23] N_{SERS} was calculated by $N_{SERS} = SA \times \rho_{SERS}$, where SA is the metal surface area contributing to the enhancement of Raman signal (**Figure S3**, Supporting Information) and ρ_{SERS} is the packing density of BZT on Au surface (6.8×10^{14} molecules cm⁻²).^[24] N_{Raman} was calculated by $N_{Raman} = A \times d_{eff} \times \rho_{BZT}$ where A is the focused illumination area, d_{eff} is an effective depth (**Figure S4**, Supporting Information), and ρ_{BZT} is the density of neat BZT (5.9×10^{21} molecules cm⁻³). It should be noted that these calculated EFs were underestimated since the calculation considered the whole metal

surface area rather than the hotspot regions and used the maximum surface density of BZT on gold. Therefore, the local SERS EFs of nanogap regions should be even higher.

Oxygen Plasma Cleaning: To assess the reusability of device, oxygen plasma cleaning was performed by a tabletop reactive ion etching system (RIE-1C, Samco, Japan) with the oxygen flow of 50 sccm and the RF power of 50 W.

Supporting Information

Supporting Information is available from the Wiley Online Library or from the author.

Acknowledgements

J.S. and W.I.N. contributed equally to this work. This work was supported by AFOSR Young Investigator Award FA9550-18-1-0328 and NIST grant 70NANB18H20. J.S. received research assistantship from Institute for Critical Technology and Applied Science (ICTAS) at Virginia Tech.

Conflict of Interest

The authors declare no conflict of interest.

Keywords

nanolaminated plasmonic crystals, SERS substrates, surface-enhanced Raman spectroscopy, vertically oriented plasmonic nanogaps

Received: December 6, 2018

Revised: January 14, 2019

Published online: February 1, 2019

- [1] a) M. Fleischmann, P. J. Hendra, A. J. Mcquillan, *Chem. Phys. Lett.* **1974**, 26, 163; b) D. L. Jeanmaire, R. P. Vanduyne, *J. Electroanal. Chem.* **1977**, 84, 1.
- [2] a) R. A. Halvorson, P. J. Vikesland, *Environ. Sci. Technol.* **2010**, 44, 7749; b) A. P. Craig, A. S. Franca, J. Irudayaraj, *Annu. Rev. Food Sci. Technol.* **2013**, 4, 369; c) X. S. Zheng, I. J. Jahn, K. Weber, D. Cialla-May, *Spectrochim. Acta, Part A* **2018**, 197, 56; d) C. Zong, M. X. Xu, L. J. Xu, T. Wei, X. Ma, X. S. Zheng, R. Hu, B. Ren, *Chem. Rev.* **2018**, 118, 4946.
- [3] P. G. Etchegoin, E. C. Le Ru, *Phys. Chem. Chem. Phys.* **2008**, 10, 6079.
- [4] E. C. Le Ru, E. Blackie, M. Meyer, P. G. Etchegoin, *J. Phys. Chem. C* **2007**, 111, 13794.
- [5] N. J. Halas, S. Lal, W. S. Chang, S. Link, P. Nordlander, *Chem. Rev.* **2011**, 111, 3913.
- [6] J. Jiang, K. Bosnick, M. Maillard, L. Brus, *J. Phys. Chem. B* **2003**, 107, 9964.
- [7] a) K. Kneipp, Y. Wang, H. Kneipp, L. T. Perelman, I. Itzkan, R. Dasari, M. S. Feld, *Phys. Rev. Lett.* **1997**, 78, 1667; b) S. M. Nie, S. R. Emery, *Science* **1997**, 275, 1102.
- [8] L. Gunnarsson, T. Rindzevicius, J. Prikulis, B. Kasemo, M. Kall, S. L. Zou, G. C. Schatz, *J. Phys. Chem. B* **2005**, 109, 1079.
- [9] a) M. Hu, F. S. Ou, W. Wu, I. Naumov, X. Li, A. M. Bratkovsky, R. S. Williams, Z. Li, *J. Am. Chem. Soc.* **2010**, 132, 12820; b) A. Kim, F. S. Ou, D. A. Ohlberg, M. Hu, R. S. Williams, Z. Li, *J. Am. Chem. Soc.* **2011**, 133, 8234; c) F. S. Ou, M. Hu, I. Naumov, A. Kim, W. Wu, A. M. Bratkovsky, X. Li, R. S. Williams, Z. Li, *Nano Lett.* **2011**, 11, 2538; d) M. S. Schmidt, J. Hubner, A. Boisen, *Adv. Mater.* **2012**, 24, OP11; e) X. Wang, S. G. Park, J. Ko, X. Xiao, V. Giannini, S. A. Maier, D. H. Kim, J. Choo, *Small* **2018**, 14, 1801623.
- [10] a) H. Im, K. C. Bantz, N. C. Lindquist, C. L. Haynes, S. H. Oh, *Nano Lett.* **2010**, 10, 2231; b) X. S. Chen, H. R. Park, M. Pelton, X. J. Piao, N. C. Lindquist, H. Im, Y. J. Kim, J. S. Ahn, K. J. Ahn, N. Park, D. S. Kim, S. H. Oh, *Nat. Commun.* **2013**, 4, 2361.
- [11] a) J. Theiss, P. Pavaskar, P. M. Echternach, R. E. Muller, S. B. Cronin, *Nano Lett.* **2010**, 10, 2749; b) Q. Fu, Z. Zhan, J. Dou, X. Zheng, R. Xu, M. Wu, Y. Lei, *ACS Appl. Mater. Interfaces* **2015**, 7, 13322; c) Z. Zhan, R. Xu, X. Zheng, Q. Fu, M. Wu, Y. Lei, *Nanotechnology* **2016**, 27, 445301.
- [12] Y. J. Oh, K. H. Jeong, *Adv. Mater.* **2012**, 24, 2234.
- [13] a) X. Zhang, Y. Zheng, X. Liu, W. Lu, J. Dai, D. Y. Lei, D. R. MacFarlane, *Adv. Mater.* **2015**, 27, 1090; b) K. Jung, J. Hahn, S. In, Y. Bae, H. Lee, P. V. Pikhitsa, K. Ahn, K. Ha, J. K. Lee, N. Park, M. Choi, *Adv. Mater.* **2014**, 26, 5924; c) M. Chirumamilla, A. Toma, A. Gopalakrishnan, G. Das, R. P. Zaccaria, R. Krahne, E. Rondanina, M. Leoncini, C. Liberale, F. De Angelis, E. Di Fabrizio, *Adv. Mater.* **2014**, 26, 2353.
- [14] a) I. Yoon, T. Kang, W. Choi, J. Kim, Y. Yoo, S. W. Joo, Q. H. Park, H. Ihee, B. Kim, *J. Am. Chem. Soc.* **2009**, 131, 758; b) M. Rycenga, X. H. Xia, C. H. Moran, F. Zhou, D. Qin, Z. Y. Li, Y. A. Xia, *Angew. Chem., Int. Ed.* **2011**, 50, 5473; c) L. Li, T. Hutter, A. S. Finomore, F. M. Huang, J. J. Baumberg, S. R. Elliott, U. Steiner, S. Mahajan, *Nano Lett.* **2012**, 12, 4242; d) S. Mubeen, S. P. Zhang, N. Kim, S. Lee, S. Kramer, H. X. Xu, M. Moskovits, *Nano Lett.* **2012**, 12, 2088; e) L. Li, T. Hutter, U. Steiner, S. Mahajan, *Analyst* **2013**, 138, 4574.
- [15] a) J. Song, W. Zhou, *Nano Lett.* **2018**, 18, 4409; b) J. Song, W. Zhou, *Conf. on Lasers and Electro-Optics*, OSA Technical Digest (online), Optical Society of America **2017**, paper FF1G.5.
- [16] J. Song, W. Zhou, *Proc. SPIE* **2017**, 10106, 1010613.
- [17] a) J. Jiang, K. Bosnick, M. Maillard, L. Brus, *J. Phys. Chem. B* **2003**, 107, 9964; b) K. Kneipp, H. Kneipp, I. Itzkan, R. R. Dasari, M. S. Feld, *J. Phys.: Condens. Matter* **2002**, 14, R597.
- [18] T. H. Joo, M. S. Kim, K. Kim, *J. Raman Spectrosc.* **1987**, 18, 57.
- [19] H. Im, K. C. Bantz, S. H. Lee, T. W. Johnson, C. L. Haynes, S. H. Oh, *Adv. Mater.* **2013**, 25, 2678.
- [20] A. C. Crawford, A. Skuratovsky, M. D. Porter, *Anal. Chem.* **2016**, 88, 6515.
- [21] J. Henzie, M. H. Lee, T. W. Odom, *Nat. Nanotechnol.* **2007**, 2, 549.
- [22] P. B. Johnson, R. W. Christy, *Phys. Rev. B* **1972**, 6, 4370.
- [23] S. Li, D. Wu, X. Xu, R. Gu, *J. Raman Spectrosc.* **2007**, 38, 1436.
- [24] a) L. J. Wan, M. Terashima, H. Noda, M. Osawa, *J. Phys. Chem. B* **2000**, 104, 3563; b) C. M. Whelan, M. R. Smyth, C. J. Barnes, *Langmuir* **1999**, 15, 116.